Induced polarization of clay-rich materials - Part 3: Partially saturated mixtures of clay and pyrite

André Revil, Ahmad Ghorbani, Zhaoyang Su, Hongzhu Cai, Xiangyun Hu

GEOPHYSICS, VOL. 89, NO. 3 (MAY-JUNE 2024); P. E101–E112, 16 FIGS., 3 TABLES.
10.1190/GEO2023-0562.1

Induced polarization of clay-rich materials — Part 3: Partially saturated mixtures of clay and pyrite

André Revil[1], Ahmad Ghorbani[2], Zhaoyang Su[3], Hongzhu Cai[4], and Xiangyun Hu[4]

ABSTRACT

Source rocks for oil and gas are often associated with shales that are rich in pyrite and kerogen. Induced polarization is a suitable tool to characterize these formations. We develop a new experimental database of 43 laboratory experiments using mixtures of clay and pyrite under fully or partially water-saturated conditions. The liquid water saturation is in the range of 20%–100%, whereas the pyrite content is in the range of 0%–17%. Spectral-induced polarization measurements are performed in the frequency range of 0.1 Hz to 45 kHz at room temperature (approximately 25°C ± 1°C). The complex conductivity spectra are fitted with a Cole-Cole model, and the Cole-Cole parameters are determined using a stochastic procedure based on a Markov chain Monte Carlo sampler. The Cole-Cole parameters associated with low-frequency dispersion are then plotted as a function of the (water) saturation and pyrite content (volume fractions). Four predictions of the model are tested against the experimental data. We find that the model is able to explain the results, including (1) the chargeability depends on the pyrite content in a predictable way, (2) the (instantaneous) conductivity depends on the saturation according to Archie's law, (3) the Cole-Cole exponent does not depend on the saturation and pyrite content (except at very small pyrite content of <1 vol%), and (4) the relaxation time is inversely proportional to the instantaneous conductivity. We also develop a more advanced petrophysical model using a double Cole-Cole distribution, in which one distribution is associated with the clay minerals and the other is associated with the pyrite.

INTRODUCTION

Induced polarization has a long history in the realm of exploration geophysics (Schlumberger, 1920; Pelton et al., 1978; Kemna et al., 2014). This method is considered a suitable approach to localize ore bodies, including in clay-rich formations (e.g., Hallof and Klein, 1983; Hall and Olhoef, 1986). Source rocks for oil and gas are often rich in pyrite, and induced polarization is a suitable tool to characterize these formations (Clavier et al., 1976; Misra et al., 2016a, 2016b). In addition, this method has also been used in hydrogeophysics to study environmental problems, including contamination plumes (Martin et al., 2020), leakages in dams and embankments (Abdulsamad et al., 2019), clay properties used for the storage of wastes (Revil, 2013a, 2013b; Mendieta et al., 2021, 2023), and in biogeophysics because of its sensitivity to roots (Zanetti et al., 2011) and bacteria (Revil et al., 2012).

A complete model describing the induced polarization properties of ore bodies immersed into porous and polarizable media has been recently described by Revil et al. (2015a, 2015b) (see also Mao and Revil, 2016a; Mao et al., 2016b; Misra et al., 2016a, 2016b; Revil et al., 2017a, 2017c). Other mechanistic models exist, including those based on the redox reactions at the surface of the metallic particles (Wong, 1979) and the polarization of the electrical double layer (Bücker et al., 2018a, 2018b). Furthermore, other models have been developed, including, for instance, empirical and semiempirical models (e.g., Dias, 2000; Gurin et al., 2015, 2019; Gurin and Titov, 2023) or models based on the differential effective medium

Manuscript received by the Editor 26 September 2023; revised manuscript received 17 December 2023; published ahead of production 26 February 2024; published online 29 April 2024.
[1]EDYTEM, Universite Grenoble Alpes, Universite Savoie Mont-Blanc, CNRS, Le Bourget du Lac, France. E-mail: andre.revil@univ-smb.fr (corresponding author).
[2]Naga Geophysics, Technolac, Le Bourget du Lac, France. E-mail: ahmad.ghorbani@naga-geophysics.com.
[3]China University of Petroleum (Beijing), State Key Laboratory of Petroleum Resources and Prospecting, Beijing, China. E-mail: 2425554377@qq.com.
[4]China University of Geosciences, School of Geophysics and Geomatics, Wuhan, China and China University of Geosciences, State Key Laboratory of Geological Processes and Mineral Resources, Wuhan, China. E-mail: caihongzhu@hotmail.com; xyhu@cug.edu.cn.

theory neglecting, however, a precise description of the underlying physicochemistry and fundamental mechanisms for the transport and storage of charge carriers (e.g., Zhdanov et al., 2012; Maineult et al., 2017, 2018; Bücker et al., 2018a, 2018b). Solving the relevant local-based Nernst-Planck equations can also be used to understand the fundamental mechanisms at play, especially the dependence of the relaxation time on the instantaneous conductivity of the material (Gurin et al., 2013, 2015; Abdulsamad et al., 2017; Revil et al., 2018, 2022; Wu et al., 2022). Only the models involving an internal polarization mechanism can explain the dependence of the relaxation time on the instantaneous conductivity of the material.

Most laboratory experiments are usually performed in saturated conditions. Some experiments have been performed with saturated sand and pyrite mixtures (Mahan et al., 1986; Hupfer et al., 2016) as well as with clay-bearing pyrite in desiccation conditions (Tartrat et al., 2019) and sand-pyrite mixtures (Martin et al., 2022). However, an integrated study of the frequency-dependent complex conductivity of a sand-pyrite mixture in an unsaturated conduction has been missing to date. In the two previous papers of this series (Revil et al., 2023a, 2023b), we study the effect of desiccation and anisotropy of mudrocks that were essentially pyrite free. We wish to extend our approach to pyrite-rich anisotropic shales, and, as a first approach, we study here synthetic isotropic mixtures made of illite, pyrite, and water.

Therefore, we propose a new set of 43 laboratory experiments to elucidate the effect of saturation and pyrite content using mixtures of illite and pyrite partially saturated by electrolyte (0.8 S m^{-1}, NaCl, 25°C) mixes, and we test further the formula proposed in the previous papers of this series (Revil et al., 2013a, 2013b). We cover the saturation range of 0.2–1.0 and the pyrite content of 0–0.17. Above a pyrite content of 0.22, the chargeability is close to one (Revil et al., 2015a, 2015b) and stays close to this value, whereas, in the range of 0–0.17, there is a rapid change in the chargeability with the pyrite content. Complex conductivity data are performed with an impedance meter in the frequency range of 0.1 Hz to 45 kHz.

MODEL

Single Cole-Cole model

We consider clay particles mixed with pyrite, as shown in Figure 1. The porous mixture is considered to be homogeneous, isotropic, and kept at a constant temperature (T_0 = 25°C). The clay and pyrite particles are polarized in a low-frequency electrical field according to the mechanisms shown in Figure 2. A small proportion of the pyrite (>3 vol%) is expected to dominate the overall polarization of these mixes. In addition, we consider that if the grain size distribution of the pyrite follows a log-normal distribution, the Cole-Cole model provides a good parametric representation of the complex conductivity of the mixture. Therefore, in this paper, the complex conductivity of such mixtures is written with a Cole-Cole parametric model initially developed for dielectrics (see Cole and Cole, 1941) as

$$\sigma^* \approx \sigma_\infty \left(1 - \frac{M}{1 + (i\omega\tau)^c}\right), \tag{1}$$

$$\sigma_0 = \sigma_\infty (1 - M), \tag{2}$$

where M denotes the chargeability (dimensionless), c is the Cole-Cole exponent (dimensionless), and τ denotes the (Cole-Cole relaxation)

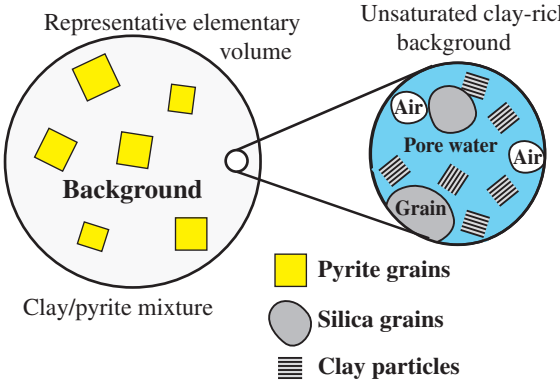

Figure 1. Sketch of the complex background and the mixture between the clay-rich background and the pyrite grains. Furthermore, the background clay-rich material is partially saturated at a partial saturation s_w. The clay particles and the pyrite grains are expected to polarize and contribute to the observed polarization of the mixture.

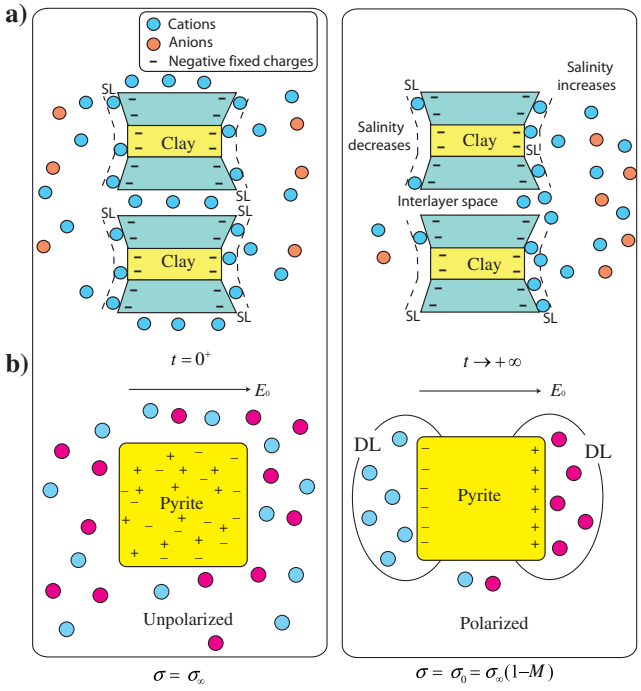

Figure 2. Induced polarization of clay particles and pyrite. (a) The surface of the clays is characterized by the presence of an electrical double layer. The applied electrical field E_0 polarizes the electrical double layer and is responsible for an induced electrical field in the direction opposed to the direction of the applied electrical field. When the external electrical field is removed, the accumulated charge will relax by electrodiffusion around the clay particle until its equilibrium state is reached. (b) Polarization of a pyrite cube. The electrodiffusion of the charge's carriers inside the grain (electrons and p-holes) polarizes the grain. A second polarization component is associated with field-induced diffuse layers (DL) in the electrolyte at the solid-liquid interface. The two sketches on the left side define the instantaneous (high-frequency) conductivity for the nonmetallic and metallic grains, whereas the figures on the right side define the DC (low-frequency) conductivity corresponding to a long application of the electrical field. The quantity M defines the chargeability (dimensionless) of the material reflecting the ability of the material to reversibly store electrical charges.

DOI:10.1190/geo2023-0562.1

time constant (expressed in s). The quantities σ_0 and σ_∞ denote the direct current (DC) and instantaneous conductivity, respectively. For the induced polarization mechanism under consideration, they correspond to the low and high asymptotic behavior of the conductivity. In time-domain induced polarization, the DC conductivity corresponds to the conductivity observed after a long application of the external electrical field and the instantaneous conductivity observed just after the application of the electrical field, respectively.

The model of Revil et al. (2015a, 2015b) (see also Mao and Revil, 2016a; Mao et al., 2016b) leads to

$$\sigma_\infty = \sigma_b(1 + 3\varphi_m), \tag{3}$$

$$M = 1 - \left(1 - \frac{9\varphi_m}{2 + 5\varphi_m + 2\varphi_m^2}\right)(1 - M_b), \tag{4}$$

where the background conductivity and chargeability are defined as

$$\sigma_b = \frac{s_w^n}{F}\sigma_w + s_w^{n-1}\sigma_S, \tag{5}$$

$$M_b = \frac{\rho_g \lambda \mathrm{CEC}}{\phi s_w \sigma_w + \rho_g B \mathrm{CEC}} \underset{s_w \to 0}{\rightarrow} R = \frac{\lambda}{B} \approx 0.10 \pm 0.02. \tag{6}$$

The surface conductivity at full saturation σ_S is defined as

$$\sigma_S = \frac{\rho_g B \mathrm{CEC}}{F\phi}. \tag{7}$$

Here, s_w denotes the liquid pore water saturation (dimensionless), φ_m denotes the volume fraction of pyrite (dimensionless), σ_w denotes the pore water conductivity (S m^{-1}), F denotes the intrinsic formation factor (dimensionless) related to the connected porosity ϕ (dimensionless) by the first Archie's law $F = \phi^{-m}$, where $m > 1$ is called the porosity or first Archie's exponent (dimensionless) (Archie, 1942) and $n > 1$ denotes the saturation exponent (dimensionless). The mobility B denotes the apparent mobility of the counterions for surface conduction (m^2 s^{-1} V^{-1}) and λ denotes the apparent mobility of the counterions for the polarization associated with the quadrature conductivity (m^2 s^{-1} V^{-1}). A dimensionless number R has also been introduced previously as $R = \lambda/B$ (for further explanations, see Revil et al., 2017b). From our previous studies (e.g., Ghorbani et al., 2018), we have β (Na$^+$, 25°C) = 3.1 ± 0.3 × 10^{-9} m^{-2} s^{-1} V^{-1}, λ (Na$^+$, 25°C) = 3.0 ± 0.7 × 10^{-10} m^{-2}s^{-1} V^{-1}, and the dimensionless number R is approximately 0.10 ± 0.02 (independent of saturation and temperature). It corresponds to an upper limit of chargeability of 100 mV/V in the absence of metallic particles.

Following Revil et al. (2022), for pyrite grains with an equivalent diameter $2a$ larger than 500 μm, the relaxation time is written as

$$\tau = \frac{a^2}{D_m}\left(1 + \frac{\sigma_S^\infty}{\sigma_b}\right) \approx a^2 \frac{\sigma_S^\infty}{D_m \sigma_b}, \tag{8}$$

where σ_S^∞ denotes the instantaneous conductivity of the pyrite grain (which is considered to be a semiconductor) and σ_b denotes the background conductivity described in equation 5. Therefore, an apparent diffusion coefficient for the relaxation time is given by $D_a = D_m \sigma_b / \sigma_S^\infty$. Because the conductivity of the grains depends on the diffusion coefficient of the charge carriers D_m, it means that D_a is independent of the diffusion coefficient of the charge carriers in the metallic particle but depends on the concentration of the charge carriers in these particles. The product of the Cole-Cole time constant by the instantaneous conductivity of the mixture is given by

$$\frac{\sigma_\infty \tau_0}{1 + 3\varphi_m} \approx \frac{a^2 e^2 C_m}{k_b T}. \tag{9}$$

The product $\sigma_\infty \tau_0/(1 + 3\varphi_m)$ should be roughly constant, or, in other words, the Cole-Cole relaxation time should be inversely proportional to the instantaneous conductivity of the mixture in the presence of pyrite. This implies, in turn, that the polarization mechanism responsible for the observed spectra is inside the grains and not on their surface. This contrasts with the explanations recently provided by Martin et al. (2022), which, in our point of view, are not consistent with the observations. Polarization mechanisms on the surface of metallic grains are physically possible (e.g., double-layer polarization and redox contributions), but they predict a different dependence of the relaxation time with the conductivity of the background.

Our goal in this paper is to check the predictive power of the previous set of equations for partially saturated clay-pyrite mixtures. This includes four predictions that are as follows:

1) The Cole-Cole exponent should be independent of the saturation and pyrite content (except for a very small amount of pyrite for which their polarization is smaller than the polarization associated with clay particles).
2) The Cole-Cole relaxation time should be inversely proportional to the instantaneous conductivity of the mixture. Martin et al. (2022, their equation 18) also notice that the relaxation time is related to the bulk electrical conductivity of the material. Gurin et al. (2015, their equation 12) also relate the relaxation time to the pore water electrical conductivity, which in turn is related to the bulk conductivity when the bulk conductivity dominates over the surface conductivity, i.e., generally at high salinities or low cation exchange capacity (CEC) materials. The CEC denotes the cation exchange capacity of the material (expressed in C kg^{-1} and often expressed in meq/100 g with 1 meq/100 g = 963.20 C kg^{-1}).
3) The dependence of the chargeability with the pyrite content should be consistent with equation 7, with the background chargeability being dependent on the saturation according to equation 9.
4) At high salinity, the (instantaneous) conductivity of the mixture follows Archie's law with the saturation, and the second Archie's exponent of the mixture n can be recovered. The dependence of the (instantaneous) conductivity of the mixture on the pyrite content should be predictable as well. At low frequencies, the conductivity of the mixtures of pyrite and illite should be smaller than the conductivity of the illite alone. This is because at low frequencies, the pyrite grains are fully polarized, and they appear as insulators.

Double Cole-Cole model

A more sophisticated way to handle the problem is to use a double Cole-Cole model. Contribution 1 is associated with the

pyrite grains. Contribution 2 is associated with the clay component. Therefore, the complex conductivity is written as

$$\sigma^* = \sigma_\infty \left(1 - \frac{M_1}{1 + (i\omega\tau_1)^{c_1}} - \frac{M_2}{1 + (i\omega\tau_2)^{c_2}}\right), \tag{10}$$

$$\sigma_\infty = \sigma_1^\infty + \sigma_2^\infty, \tag{11}$$

$$\sigma_0 = \sigma_\infty (1 - M_1 - M_2), \tag{12}$$

where we use the same notations as previously for the chargeabilities, the Cole-Cole exponents, and the Cole-Cole relaxation times. The total chargeability is defined as

$$M = \frac{\sigma_\infty - \sigma_0}{\sigma_\infty} = M_1 + M_2. \tag{13}$$

We can easily write the two chargeability contributions as

$$M_1 = \frac{9\varphi_m}{2 + 5\varphi_m + 2\varphi_m^2}, \tag{14}$$

$$M_2 = \frac{\rho_g \lambda \mathrm{CEC}}{\phi s_w \sigma_w + \rho_g B \mathrm{CEC}}. \tag{15}$$

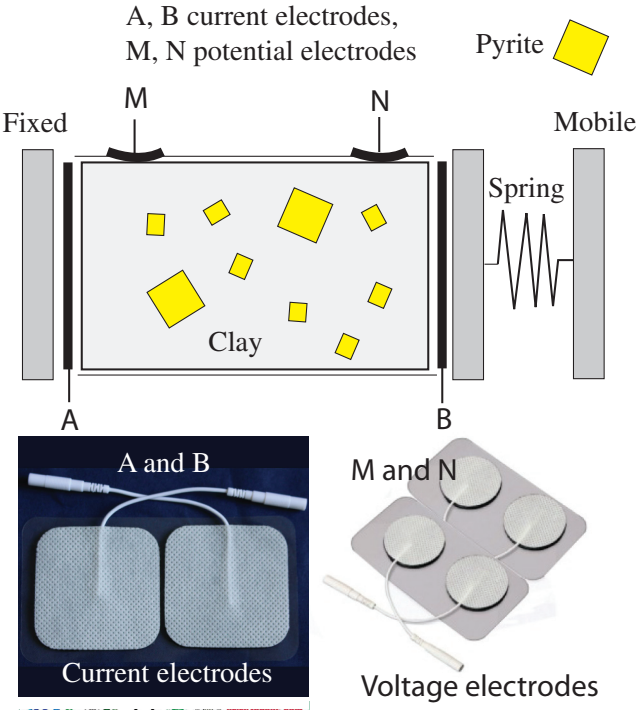

Figure 3. Experimental setup for the complex conductivity spectra. The electrodes are self-adhesive super-conductive carbon film, carbon/Ag/AgCl electrodes with biocompatible hydrogel. The sample (mix of illite and pyrite) is contained in a plastic tube with the pyrite cubes contained in between the voltage electrodes M and N. The electrodes A and B denote the current electrodes.

Equations 13–15 are consistent with equation 4 when the chargeability of the background is always much smaller than one (remember that $M_2 < R = 0.10$). The instantaneous conductivity and DC conductivity of the background material are written as, respectively,

$$\sigma_2^\infty = \frac{1}{F} s_w^n \sigma_w + \left(\frac{1}{F\phi}\right) s_w^{n-1} \rho_g B \mathrm{CEC}, \tag{16}$$

$$\sigma_2^0 = \frac{1}{F} s_w^n \sigma_w + \left(\frac{1}{F\phi}\right) s_w^{n-1} \rho_g (B - \lambda) \mathrm{CEC}, \tag{17}$$

which are consistent with equation 15 and the definition of $M_2 = (\sigma_2^\infty - \sigma_2^0)/\sigma_2^\infty$. Because we have $\sigma_\infty = \sigma_2^\infty(1 + 3\varphi_m)$ and $\sigma_\infty = \sigma_1^\infty + \sigma_2^\infty$, this yields $\sigma_1^\infty = 3\varphi_m \sigma_2^\infty$. The exponents c_1 and c_2 and the relaxation times τ_1 and τ_1 can be determined through the fit of the complex conductivity spectra. The advantage of using a double Cole-Cole model is that we can first fit the Cole-Cole model for the background material (component 2) and then keep this component unchanged when dealing with the mixtures.

MATERIALS AND METHODS

We performed complex conductivity measurements with a high-precision impedance meter, namely the ZEL-SIP04-V02 (Zimmermann et al., 2007, 2008). The complex conductivity spectra were obtained in the frequency range between 0.1 Hz and 45 kHz at room temperature (approximately 25°C). A sketch of the experimental setup is shown in Figure 3, and we follow the approach discussed in the two previous papers of this series (Revil et al., 2013a, 2013b). The measured impedance was converted into complex conductivity using the geometric factor calculated based on the geometry of the sample holder and the position of the ABMN electrodes (AB denotes the current electrodes, and MN denotes the voltage electrodes).

The (background) clay material is a natural illitic material. Its CEC was determined using the cobalt hexamine chloride method (Guillaume, 2002). We found CEC = 9.74 meq/100 g or 9402 C/kg (two replicates) (Table 1). The complex conductivity spectra of the illite alone were first obtained at the four pore water solutions

Table 1. Properties of the background material used in the present study (illite).

Property	Value
CEC (meq/100 g)	9.74
ρ_g (kg m^{-3})	2650
ϕ	0.65
F	2.1
σ_S (S m^{-1})	2×10^{-2}
n	1.4 ± 0.2
M_b	0.015

The CEC has been obtained with the cobalthexamine method. The porosity was obtained using the dry and saturated weights of the sample and its volume. The formation factor and the surface conductivity are obtained from the electrical conductivity measurements at three pore water salinities (1 Hz, NaCl, 25°C). The saturation exponent n is obtained using conductivity measurements at different saturations. The chargeability of the background material M_b was also measured at saturation. The grain density ρ_g is close to the grain density of silica.

at 25°C (NaCl). The conductivity (at 1 Hz) is shown in Figure 4a. The formation factor F and surface conductivity $\sigma_S = \rho_g B\mathrm{CEC}/F\phi$ are determined by fitting the conductivity equation for the background to these data, and the values are reported in Table 1. The formation factor F is 2.1, and the surface conductivity is 0.021 S m^{-1}. We can check that the value of the surface conductivity is consistent with the value of the CEC and formation factor. Using equation 7, $\sigma_S = \rho_g B\mathrm{CEC}/F\phi$ and with a grain density $\rho_g = 2650$ kg m^{-3}, $F = 2.1$, $\phi = 0.65$, CEC = 9401.5 C kg^{-1}, and β (Na$^+$, 25°C) = 3.1 $\pm$ 0.3 $\times$ 10^{-9} m^{2}s^{-1} V^{-1}, we obtain a surface conductivity of 5.6 $\times$ 10^{-2} S m^{-1}, slightly larger than the measured value of 2.1 $\times$ 10^{-2} S m^{-1}.

We also performed complex conductivity experiments to study the saturation behavior of the background properties. The dependence of the background conductivity and background chargeability on the saturation is provided in Table 2 and shown in Figure 4b. The background conductivity follows Archie's type behavior with a low

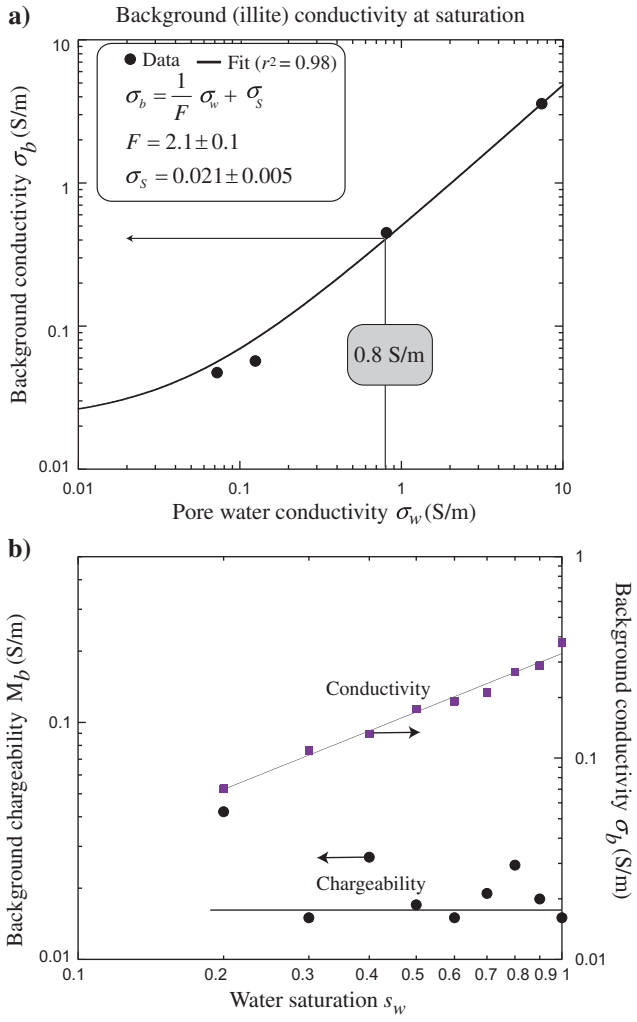

Figure 4. Properties of the background. (a) Electrical conductivity of the background material (illite, 1 Hz) versus the pore water conductivity using four electrolytes (NaCl, 25°C). The plain line denotes a fit of the linear conductivity model to determine the formation factor and the surface conductivity. In this paper, the experiment for the illite/pyrite mixtures is performed with an electrolyte at 0.8 S m^{-1} (25°C, NaCl). This yields a background conductivity σ_b of 0.40 S m^{-1}. (b) Chargeability and conductivity versus saturation ($n = 1.0 \pm 0.1$, $r^2 = 0.96$). The background chargeability data are too scattered to be fitted. The plain line corresponds to a constant background chargeability of 0.015.

Table 2. Dependence of the background chargeability and conductivity on saturation.

Saturation s_w	M_b	σ_b
1.0	0.015	0.3760
0.9	0.018	0.2876
0.8	0.025	0.2681
0.7	0.019	0.2118
0.6	0.015	0.1914
0.5	0.017	0.1756
0.4	0.027	0.1319
0.3	0.015	0.1088
0.2	0.042	0.0705

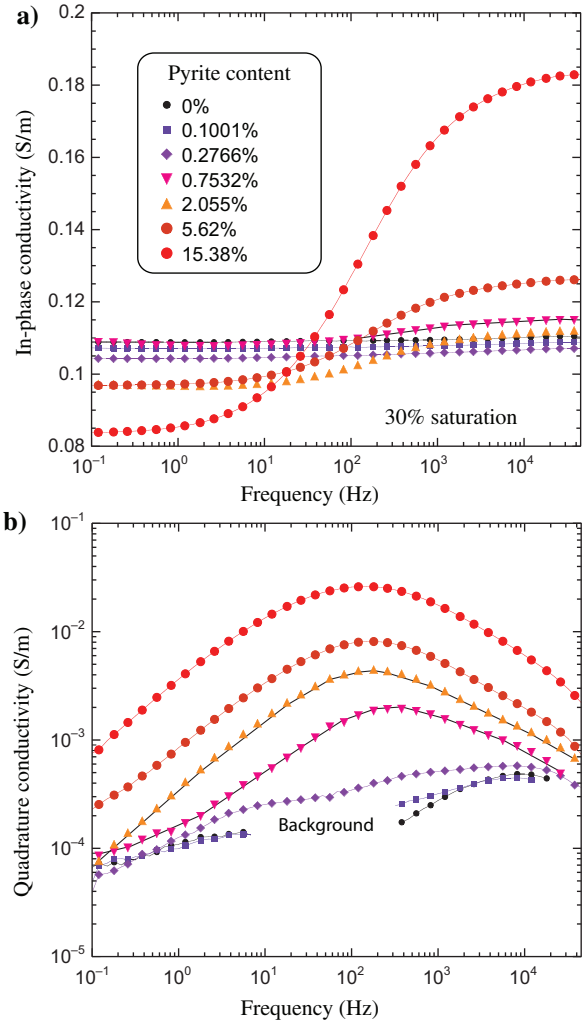

Figure 5. (a and b) Example of complex conductivity spectra for a given water saturation (30%) and various pyrite contents. The lines are guides for the eyes.

Table 3. Low-frequency Cole-Cole parameters for the different experiments performed in this paper fitted with a single Cole-Cole parametric model.

Experiment	s_w	ϕ_m	c	σ_∞ (S m^{-1})	τ (10^{-4} s)	M
E1	0.2	0	0.46	0.0705	5.67	0.01
E2	0.2	0.0074	0.55	0.0878	9.97	0.053
E3	0.2	0.0202	0.65	0.0892	12.2	0.145
E4	0.2	0.055	0.69	0.1007	18.5	0.208
E5	0.2	0.1508	0.74	0.1402	21.7	0.318
E6	0.3	0.0075	0.65	0.1182	4.7	0.056
E7	0.3	0.0206	0.71	0.1132	10.1	0.118
E8	0.3	0.0562	0.68	0.1275	12.4	0.154
E9	0.3	0.1538	0.68	0.1853	24.5	0.326
E10	0.4	0.001	0.64	0.1327	20	0.01
E11	0.4	0.028	0.61	0.1366	6	0.03
E13	0.4	0.077	0.62	0.1421	5.2	0.058
E14	0.4	0.0208	0.79	0.143	7.8	0.083
E15	0.4	0.0568	0.6	0.1621	10.3	0.127
E16	0.4	0.1402	0.54	0.1875	11.7	0.151
E17	0.5	0	0.51	0.184	1.5	0.011
E18	0.5	0.001	0.76	0.193	3.4	0.011
E19	0.5	0.028	0.42	0.168	1.4	0.013
E20	0.5	0.077	0.69	0.188	8	0.051
E21	0.5	0.021	0.73	0.184	4.7	0.075
E22	0.5	0.058	0.73	0.214	8.4	0.213
E23	0.5	0.156	0.73	0.361	9.1	0.409
E24	0.6	0.0077	0.64	0.204	6	0.055
E25	0.6	0.0209	0.83	0.17	7.6	0.068
E26	0.6	0.0574	0.79	0.256	17.7	0.137
E27	0.6	0.1564	0.72	0.342	14.7	0.238
E28	0.7	0.0077	0.58	0.229	4.5	0.06
E29	0.7	0.0209	0.63	0.245	5.3	0.103
E30	0.7	0.0581	0.74	0.285	7.1	0.202
E31	0.7	0.1583	0.72	0.495	10.1	0.342
E32	0.8	0.0076	0.59	0.303	4.7	0.041
E33	0.8	0.0209	0.71	0.344	9.3	0.106
E34	0.8	0.0572	0.71	0.372	6.7	0.211
E35	0.8	0.1548	0.74	0.646	8.7	0.307
E36	0.9	0.0077	0.6	0.319	3.9	0.051
E37	0.9	0.0212	0.65	0.367	5.2	0.084
E38	0.9	0.058	0.57	0.361	5	0.361
E39	0.9	0.1582	0.74	0.643	14	0.642
E40	1	0.0081	0.63	0.43	5.5	0.069
E41	1	0.0225	0.69	0.46	3.9	0.117
E42	1	0.0612	0.74	0.477	10.5	0.7
E43	1	0.1666	0.63	1.114	3.7	0.338

The experiments are labeled as E1–E43. The quantities s_w and ϕ_m denote the saturation and the pyrite content (weight fraction), respectively. The quantities c and σ_∞ denote the Cole-Cole exponent and the instantaneous conductivity, respectively. Finally, the quantities τ and M denote the Cole-Cole relaxation time and the chargeability, respectively. The samples are saturated with an electrolyte at a pore water conductivity of 0.8 S m^{-1} (NaCl, 25°C).

value of the saturation exponent n close to one. The background chargeability seems to increase slightly with the decrease in the saturation but the scatter in the data points does not allow to properly fit these data with the model discussed previously.

This illite is mixed with pyrite cubes of various sizes to obtain the desired metal content φ_m in the range of 0%–17%. The volume of pyrite is first determined by immersion. Then, all of the experiments performed in this paper (see Table 3) were done with a pore water conductivity of 0.8 S m^{-1} (NaCl, 25°C). For the experiments, a homogeneous mixture was prepared with the background clay, the electrolyte at 0.8 S m^{-1}, and the desired saturation and pyrite cubes to mimic the mixture shown in Figure 1. Once prepared, we closed the core sample holders (Figure 2) and let them rest for approximately 10 days. A total of 43 experiments (reported in Table 3) are performed.

A typical set of complex conductivity spectra is shown in Figure 5 at a given saturation (30% in this case). The data show a clear polarization that increases with the increase in the pyrite content, as expected. These data can be fitted by a Cole-Cole model, and we use a Markov chain Monte Carlo (MCMC) sampler to fit the Cole-Cole parameters for each complex conductivity spectrum. The values of the Cole-Cole parameters are reported in Table 3. The fit of the complex conductivity spectra is shown in Figures 6, 7, 8, 9, and 10. We can say that the Cole-Cole model provides a good descriptor of the polarization effect. Then, in the next section, we discuss the dependence of the Cole-Cole parameters on the properties of the mixtures.

RESULTS

Single Cole-Cole model

First, in Figure 11, we check that the Cole-Cole exponent c is independent of the saturation and pyrite content (except for small pyrite content <1 vol% for which we recover the Cole-Cole exponent that is associated with an illite of approximately 0.50, not shown here). Because the Cole-Cole exponent described the broadness of the polarization length scales, this is not surprising.

In Figure 12, the Cole-Cole relaxation time is plotted as a function of the instantaneous conductivity. We observe, despite the scatter in the data, that the Cole-Cole relaxation time is inversely proportional to the instantaneous conductivity of the material. In Figure 13, we plot the chargeability of the mixture as a function of the pyrite content. We check that the data

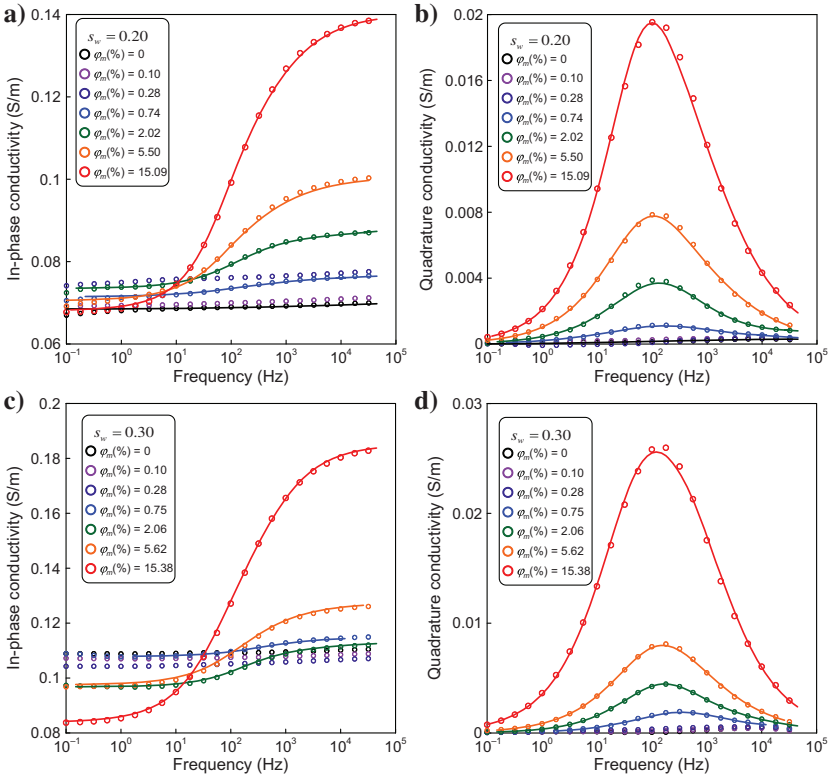

Figure 6. Cole-Cole fit of the complex conductivity spectra. (a) In-phase conductivity data at a partial water saturation of 20%, (b) quadrature conductivity data at a partial water saturation of 20%, (c) in-phase conductivity data at a partial water saturation of 30%, and (d) quadrature conductivity data at a partial water saturation of 30%. The plain lines define the best fit of the Cole-Cole model used to fit the spectra with the highest pyrite contents (above 0.5%).

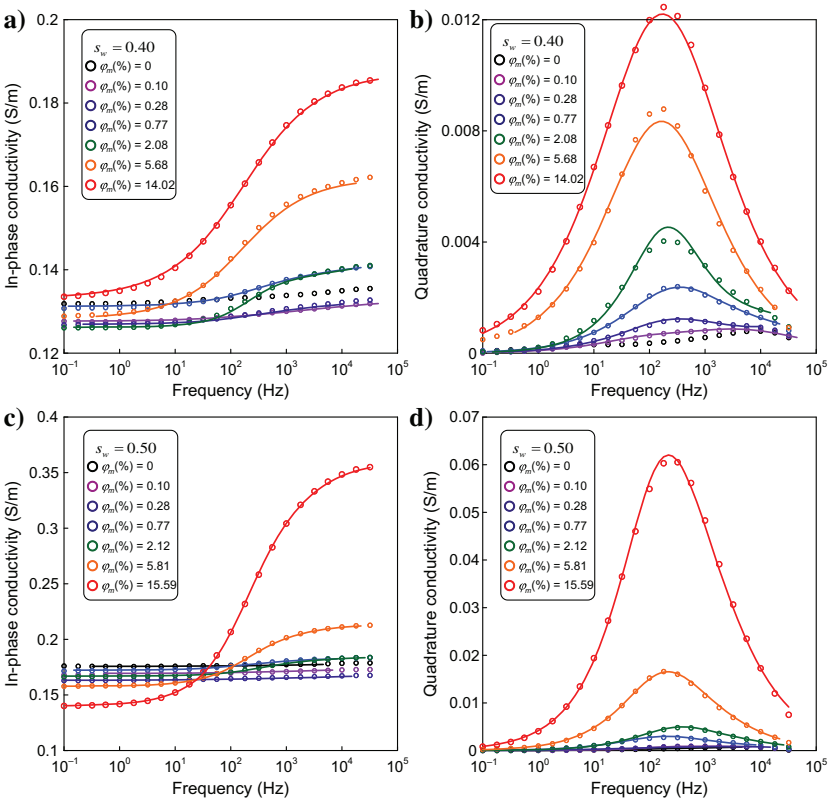

Figure 7. Cole-Cole fit of the complex conductivity spectra. (a) In-phase conductivity data at a partial water saturation of 40%, (b) quadrature conductivity data at a partial water saturation of 40%, (c) in-phase conductivity data at a partial water saturation of 40%, and (d) quadrature conductivity data at a partial water saturation of 40%. The plain lines define the best fit of the Cole-Cole model used to fit the spectra with the highest pyrite contents (above 0.5%).

DOI:10.1190/geo2023-0562.1

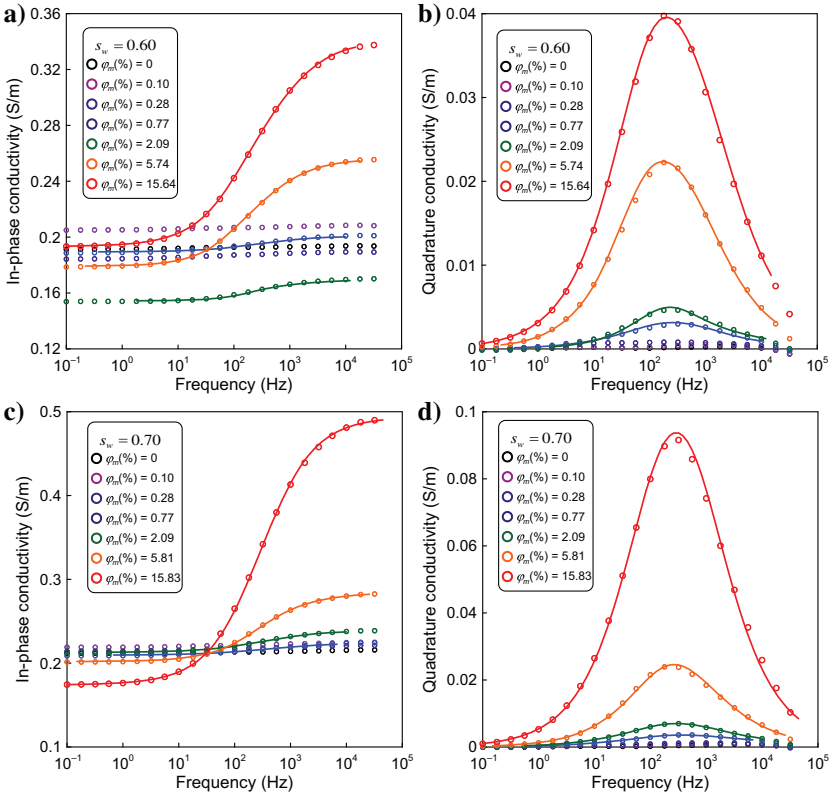

Figure 8. Cole-Cole fit of the complex conductivity spectra. (a) In-phase conductivity data at a partial water saturation of 60%, (b) quadrature conductivity data at a partial water saturation of 60%, (c) in-phase conductivity data at a partial water saturation of 70%, and (d) quadrature conductivity data at a partial water saturation of 70%. The plain lines define the best fit of the Cole-Cole model used to fit the spectra with the highest pyrite contents (above 0.5%).

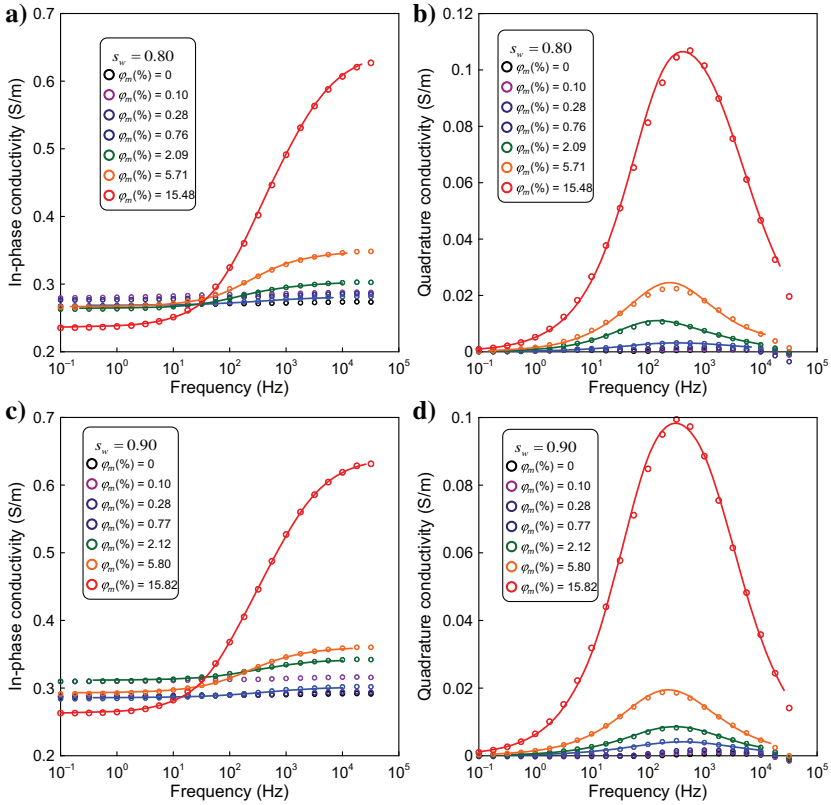

Figure 9. Cole-Cole fit of the complex conductivity spectra. (a) In-phase conductivity data at a partial water saturation of 80%, (b) quadrature conductivity data at a partial water saturation of 80%, (c) in-phase conductivity data at a partial water saturation of 90%, and (d) quadrature conductivity data at a partial water saturation of 90%. The plain lines define the best fit of the Cole-Cole model used to fit the spectra with the highest pyrite contents (above 0.5%).

are grossly consistent with the prediction of the model given in equation 4.

In Figure 14a and 14b, we plot the instantaneous conductivity as a function of the saturation at low and high pyrite contents. We check, in agreement with the model, that the dependence on saturation of the instantaneous conductivity does not depend on the pyrite content. In Figure 15, we check that the increase in the instantaneous conductivity with the pyrite content is grossly consistent with the prediction of the model. Note that the value of the saturation exponent n we found is low (n = 1.25) but inside the range of realistic values (n comprised between 1 and 4).

Double Cole-Cole model

We use a stochastic approach to fit the double Cole-Cole model, but we use specific relationships to account for the underlying physics. We use the following complex conductivity equation:

$$\sigma^* = \sigma_\infty(s_w,\varphi_m)\left(1-\frac{\frac{9\varphi_m}{2+5\varphi_m+2\varphi_m^2}}{1+i\omega\left(\frac{\tilde{\tau}_1}{\sigma_\infty(s_w,\varphi_m)}\right)^{c_1}}-\frac{\frac{\rho_g\lambda\mathrm{CEC}}{\phi s_w\sigma_w+\rho_g B\mathrm{CEC}}}{1+(i\omega\tau_2)^{c_2}}\right), \quad (18)$$

where we used the following expression for the instantaneous conductivity of the mixture:

$$\sigma_\infty = (1+3\varphi_m)\left[\frac{1}{F}s_w^n\sigma_w+\left(\frac{1}{F\phi}\right)s_w^{n-1}\rho_g B\mathrm{CEC}\right]. \quad (19)$$

The input parameters are the complex conductivity spectra, the saturation s_w, and the pyrite content φ_m. The parameter c_2 is determined by the absence of pyrite using the complex conductivity spectra for illite alone (c_2 close to 0.5). The parameters to optimize are the Cole-Cole exponent c_1, the second Archie's exponent n, and the reduced relaxation time $\tilde{\tau}_1 = \tau_1\sigma_\infty(s_w,\varphi_m)$, so there are only three parameters. The other parameters, F, ϕ, CEC, and ρ_g, are provided in Table 1. Finally, we use β (Na^+, 25°C) = 3.1 ± 0.3 × 10^{-9} m^{-2} s^{-1} V^{-1} and λ (Na^+, 25°C) = 3.0 ± 0.7 × 10^{-10} m^{-2} s^{-1} V^{-1} for the two mobilities and a pore water conductivity $\sigma_w = 0.8$ S m^{-1} (NaCl, 25°C).

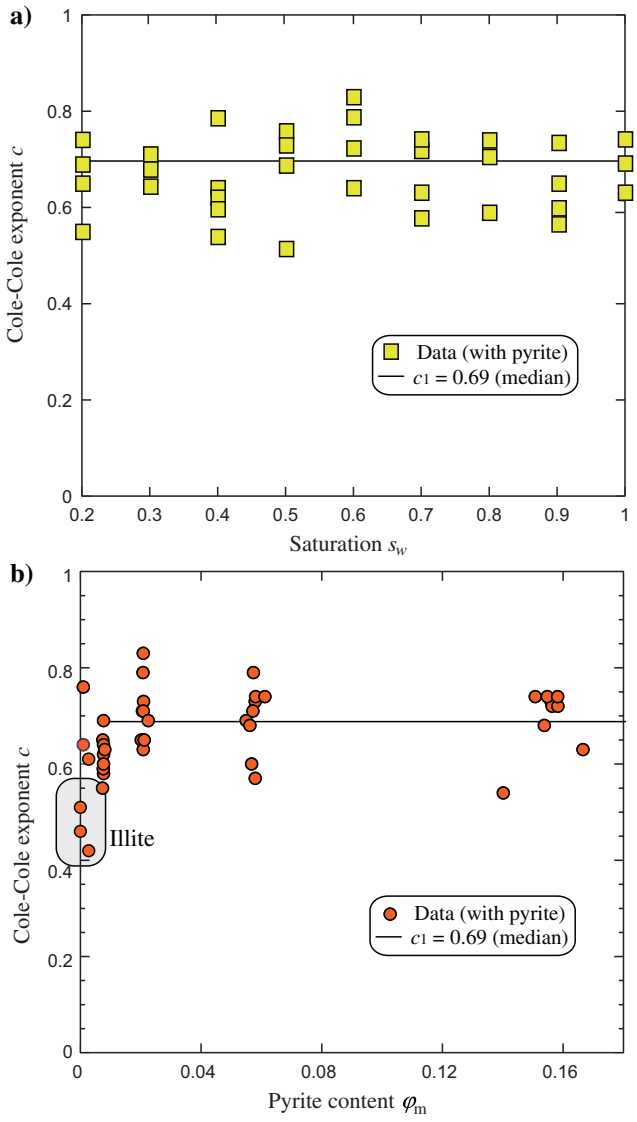

Figure 11. Cole-Cole exponent. (a) Cole-Cole exponent versus water saturation. As predicted by the theory, we observe that the Cole-Cole exponent does not depend on saturation. We have removed the data of experiments E1 and E17 (no pyrite, pure illite $c \approx 0.50 \pm 0.01$). (b) Cole-Cole exponent versus pyrite content. The Cole-Cole exponent reflects the distribution of the grain sizes of the pyrite. The plain line denotes the median value of the Cole-Cole exponent for the experimental data.

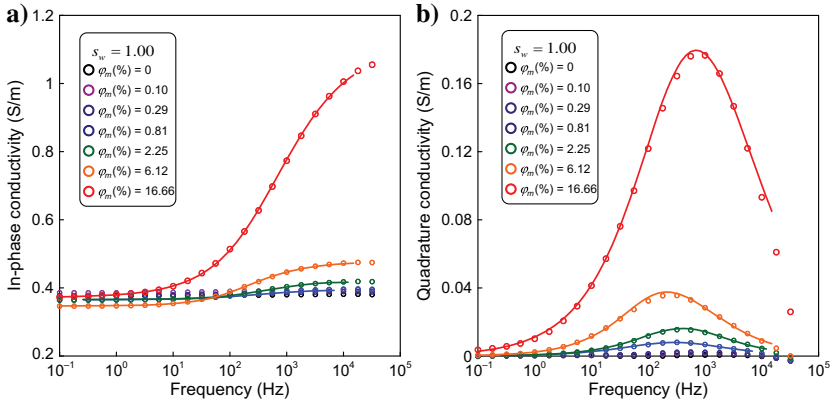

Figure 10. Cole-Cole fit of the complex conductivity spectra. (a) In-phase conductivity data at saturation and (b) quadrature conductivity data at saturation. The plain lines define the best fit of the Cole-Cole model used to fit the spectra with the highest pyrite contents (above 0.5%).

A comparison between the double Cole-Cole model and the experimental data for saturation of 20% is shown in Figure 16. The model is able to explain the data, but the fits are not perfect. With a relaxation time of $\tau_2 = 2 \times 10^{-4}$ s (for the entire data set), we obtain the following values for the three other parameters: $c_1 = 0.7 \pm 0.2$, $n = 1.9 \pm 0.7$, and the reduced relaxation time $\tilde{\tau}_1 = 2.2 \pm 0.9$ S m^{-1} for pyrite. The value of c_1 is what we expect from Figure 11b. The value of n conforms to the expected value for the saturation exponent, generally close to the cementation exponent m. Finally, the value of $\tilde{\tau}_1$ is very well determined with a small standard deviation indicating that the relaxation time τ_1 is indeed inversely proportional to the conductivity of the material.

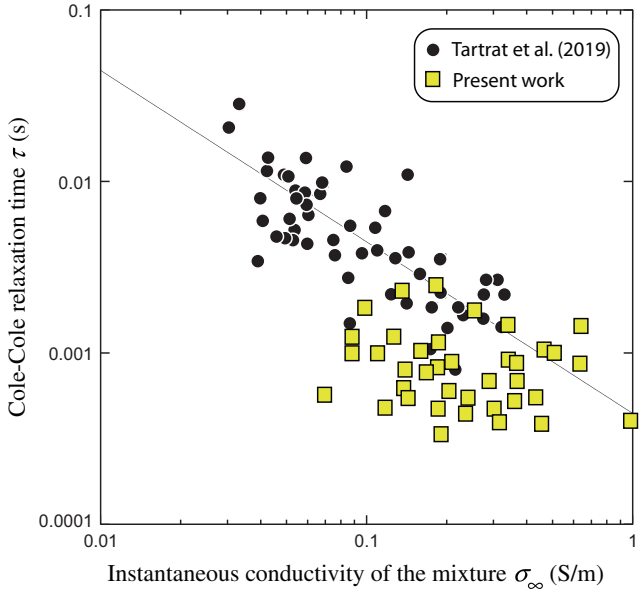

Figure 12. Evolution of the low-frequency Cole-Cole relaxation time versus the water saturation. A comparison is made with the data of Tartrat et al. (2019) using the same illite but for desiccation experiments. The conductivity of the background shows an effect on the Cole-Cole relaxation time. The plain line corresponds to the fit of the data from Tartrat et al. (2019).

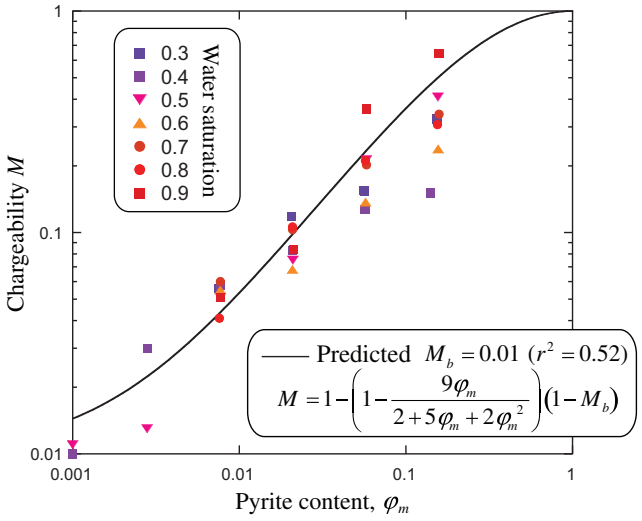

Figure 13. Evolution of the chargeability versus the pyrite content. The plain line represents the fit done with equation 4. We do not see an effect of the water saturation in the data. The low value of the background chargeability M_b is due to the relatively high pore water conductivity used in the present study (0.8 S m^{-1}). Despite the dispersion of the data set, the overall trend is relatively well reproduced in the data.

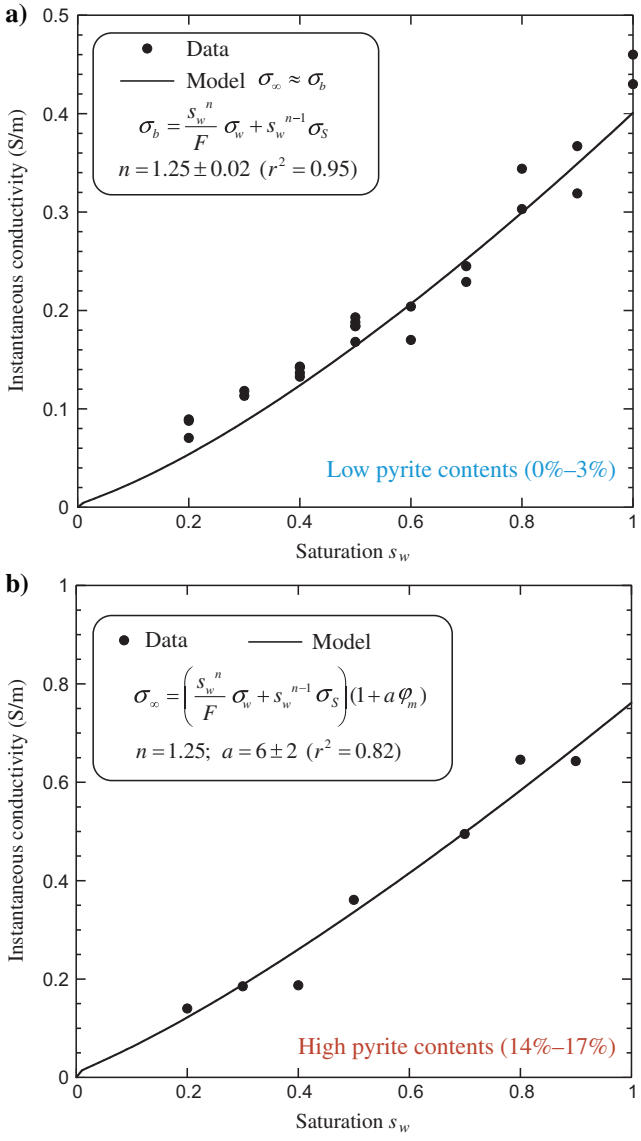

Figure 14. Dependence of the instantaneous conductivity σ_∞ with saturation s_w. (a) For mixtures with pyrite content smaller or equal to 3% versus the saturation. (b) For mixtures with pyrite content in the range of 14%–17%. The pore water conductivity is 0.8 S m^{-1} (NaCl, 25°C). The values used for the surface conductivity and formation factor are those of Table 1. We observe that the value of the saturation exponent remains the same ($n = 1.25$) for the two ranges of pyrite contents (high and low).

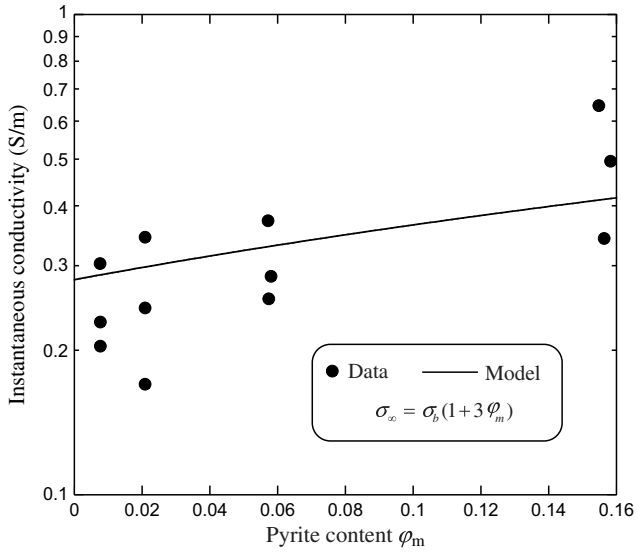

Figure 15. Dependence of the instantaneous conductivity σ_∞ of the illite/pyrite mixtures as a function of the pyrite content for the water saturation in the range of 60%–80%. The plain line corresponds to the trend predicted by the theory.

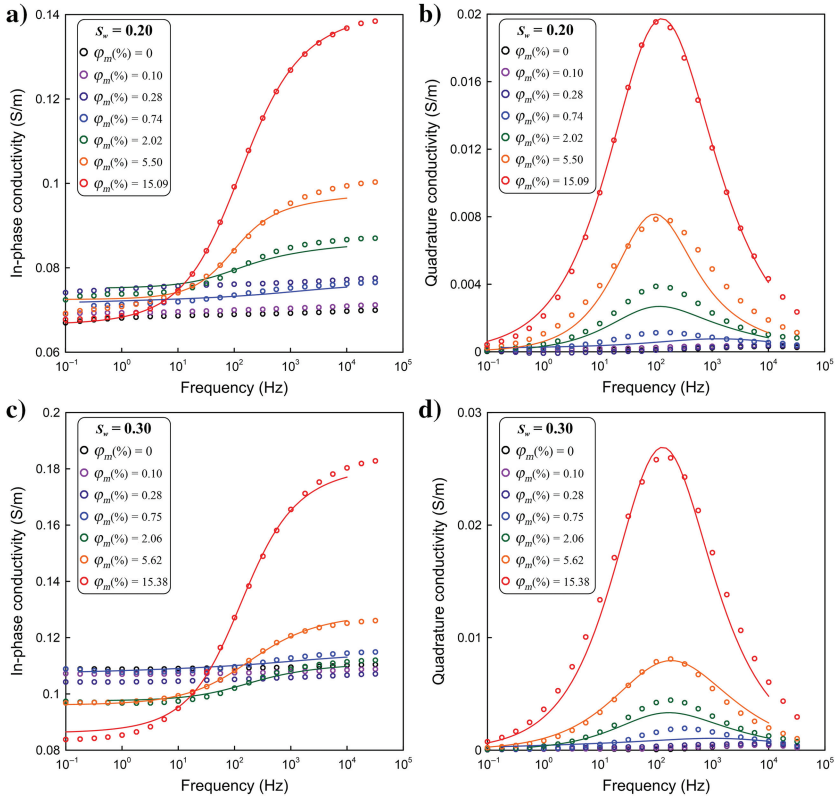

Figure 16. Comparison between the double Cole-Cole model and the experimental data at a saturation of 20%. (a) In-phase conductivity data at 20% saturation. (b) Quadrature conductivity data at 20% saturation. (c) In-phase conductivity data at 30% saturation. (d) Quadrature conductivity data at 30% saturation.

CONCLUSION

We performed complex conductivity experiments on 43 mixtures of illite/pyrite and an electrolyte to study the effect of the pyrite content and saturation. The complex conductivity spectra can be accurately fitted with a single Cole-Cole model at least above a critical content of pyrite or a double Cole-Cole model accounting for the polarization spectra of the clay particles and pyrite grains. The Cole-Cole parameters are given physical interpretation thanks to a mechanistic model. We check that the Cole-Cole exponents do not depend on the saturation. The instantaneous conductivity depends on the saturation according to a power law relationship with a power law exponent given by the second Archie's exponent n. The chargeability depends linearly on the pyrite content, with a background chargeability that depends on the saturation. Finally, the Cole-Cole relaxation time is inversely proportional to the instantaneous conductivity, which depends on saturation in a predictable way. The proposed double Cole-Cole model represents a step forward in being able to model such complex mixtures accounting for a few textural parameters and state variables.

In the future, we could check if the data obtained in the course of this analysis could be compared with numerical experiments using a network approach. We will also apply our approach to real source rocks that are rich in pyrite and kerogen also accounting for their anisotropy. If we can explain the polarization characteristic of such complex media quantitatively, this means that we could interpret the field data for any complex situation in oil reservoirs and source rocks.

ACKNOWLEDGMENTS

We thank E. Zimmerman at Forschungszentrum Jülich for developing and building the low-frequency impedance spectrometer used here. We also thank the editor X. Garcia and the three reviewers for their time and useful comments that improved our manuscript. This work is partially funded through the PALLAS project.

DATA AND MATERIALS AVAILABILITY

Data associated with this research are available and can be obtained by contacting the corresponding author.

REFERENCES

Abdulsamad, F., N. Florsch, and C. Camerlynck, 2017, Spectral induced polarization in a sandy medium containing semiconductor materials: Experimental results and numerical modelling of the polarization mechanism: Near Surface Geophysics, **15**, 669–683, doi: 10.3997/1873-0604.2017052.

Abdulsamad, F., A. Revil, A. Soueid Ahmed, A. Coperey, M. Karaoulis, S. Nicaise, and L. Peyras, 2019, Induced polarization tomography applied to the detection and the monitoring of leaks in embankments dams and dikes: Engineering Geology, **254**, 89–101, doi: 10.1016/j.enggeo.2019.04.001.

Archie, G. E., 1942, The electrical resistivity log as an aid in determining some reservoir characteristics: Transactions of the American Institute of Mining and Metallurgical Engineers, **146**, 54–62, doi: 10.2118/942054-G.

Bücker, M., A. Flores Orozco, and A. Kemna, 2018a, Electrochemical polarization around metallic particles — Part 1: The role of diffuse-layer and volume-diffusion relaxation: Geophysics, **83**, no. 4, E203–E217, doi: 10.1190/geo2017-0401.1.

Bücker, M., S. Undorf, A. Flores Orozco, and A. Kemna, 2018b, Electrochemical polarization around metallic particles — Part 2: The role of diffuse-surface charge: Geophysics, **84**, no. 2, E57–E73, doi: 10.1190/geo2018-0150.1.

Clavier, C., A. Heim, and C. Scala, 1976, Effect of pyrite on resistivity and other logging measurements: 17th Annual Logging Symposium, SPWLA, Extended Abstracts.

Cole, K. S., and R. H. Cole, 1941, Dispersion and absorption in dielectrics: Journal of Chemical Physics, **9**, 341–351, doi: 10.1063/1.1750906.

Dias, C. A., 2000, Developments in a model to describe low-frequency electrical polarization of rocks: Geophysics, **65**, 437–451, doi: 10.1190/1.1444738.

Ghorbani, A., A. Revil, A. Coperey, A. Soueid Ahmed, S. Roque, J. M. Heap, H. Grandis, and F. Viveiros, 2018, Complex conductivity of volcanic rocks and the geophysical mapping of alteration in volcanoes: Journal of Volcanology and Geothermal Research, **357**, 106–127, doi: 10.1016/j.jvolgeores.2018.04.014.

Guillaume, D., 2002, Etude expérimentale du système fer-smectite en présence de solution à 80°C et 300°C: Ph.D. thesis, Université Henri Poincaré — Nancy 1.

Gurin, G., A. Tarasov, Y. Ilyin, and K. Titov, 2013, Time domain spectral induced polarization of disseminated electronic conductors: Laboratory data analysis through the Debye decomposition approach: Journal of Applied Geophysics, **98**, 44–53, doi: 10.1016/j.jappgeo.2013.07.008.

Gurin, G., and K. Titov, 2023, Spectral induced polarization of rocks with electronically conductive inclusions: A semi-empirical capillary model: Geophysical Journal International, **234**, 1722–1734, doi: 10.1093/gji/ggad157.

Gurin, G., K. Titov, and Y. Ilyin, 2019, Induced polarization of rocks containing metallic particles: Evidence of passivation effect: Geophysical Research Letters, **46**, 670–677, doi: 10.1029/2018GL080107.

Gurin, G., K. Titov, Y. Ilyin, and A. Tarasov, 2015, Induced polarization of disseminated electronically conductive minerals: A semi-empirical model: Geophysical Journal International, **200**, 1555–1565, doi: 10.1093/gji/ggu490.

Hall, S. H., and G. R. Olhoef, 1986, Nonlinear complex resistivity of some nickel sulfides from Western Australia: Geophysical Prospecting, **34**, 1255–1276, doi: 10.1111/j.1365-2478.1986.tb00527.x.

Hallof, P. G., and J. D. Klein, 1983, Electrical parameters of volcanogenic mineral deposits in Ontario, *in* R. B. Barlow and E. G. Pye, eds., Exploration technology development program of the board of industrial leadership and development: Ontario Geological Survey, 11–26.

Hupfer, S., T. Martin, A. Weller, K. Kuhn, T. Günther, V. Djotsa, and U. Noell, 2016, Polarization effects of unconsolidated sulphide-sand-mixtures: Journal of Applied Geophysics, **135**, 456–465, doi: 10.1016/j.jappgeo.2015.12.003.

Kemna, A., J. Huisman, E. Zimmermann, R. Martin, Y. Zhao, A. Treichel, A. Flores Orozco, and T. Fechner, 2014, Broadband electrical impedance tomography for subsurface characterization using improved corrections of electromagnetic coupling and spectral regularization, *in* M. Weber and U. Münch, eds., Tomography of the earth's crust: From geophysical sounding to real-time monitoring: Springer, 1–20.

Mahan, M. K., J. D. Redman, and D. W. Strangway, 1986, Complex resistivity of synthetic sulfide bearing rocks: Geophysical Prospecting, **34**, 743–768, doi: 10.1111/j.1365-2478.1986.tb00491.x.

Maineult, A., D. Jougnot, and A. Revil, 2018, Variations of petrophysical properties and spectral induced polarization in response to drainage and imbibition: A study on a correlated random tube network: Geophysical Journal International, **212**, 1398–1411, doi: 10.1093/gji/ggx474.

Maineult, A., A. Revil, C. Camerlynck, N. Florsch, and K. Titov, 2017, Upscaling of spectral induced polarization response using random tube networks: Geophysical Journal International, **209**, 948–960, doi: 10.1093/gji/ggx066.

Mao, D., and A. Revil, 2016a, Induced polarization response of porous media with metallic particles. — Part 3. A new approach to time-domain induced polarization tomography: Geophysics, **81**, no. 4, D345–D357, doi: 10.1190/geo2015-0283.1.

Mao, D., A. Revil, and J. Hinton, 2016b, Induced polarization response of porous media with metallic particles. — Part 4. Detection of metallic and nonmetallic targets in time-domain-induced polarization tomography: Geophysics, **81**, no. 4, D359–D375, doi: 10.1190/geo2015-0480.1.

Martin, T., K. Kuhn, T. Günther, and R. Kniess, 2020, Geophysical exploration of a historical stamp mill dump for the volume estimation of valuable residues: Journal of Environmental and Engineering Geophysics, **25**, 275–286, doi: 10.2113/JEEG19-080.

Martin, T., A. Weller, and L. Behling, 2022, Desaturation effects of pyrite–sand mixtures on induced polarization signals: Geophysical Journal International, **228**, 275–290, doi: 10.1093/gji/ggab333.

Mendieta, A., D. Jougnot, P. Leroy, and A. Maineult, 2021, Spectral induced polarization characterization of non-consolidated clays for varying salinities — An experimental study: Journal of Geophysical Research: Solid Earth, **126**, e2020JB021125, doi: 10.1029/2020JB021125.

Mendieta, A., A. Maineult, P. Leroy, and D. Jougnot, 2023, Spectral induced polarization of heterogeneous non-consolidated clays: Geophysical Journal International, **233**, 436–447, doi: 10.1093/gji/ggac466.

Misra, S., C. Torres-Verdín, A. Revil, J. Rasmus, and D. Homan, 2016a, Interfacial polarization of disseminated conductive minerals in absence of redox-active species — Part 1: Mechanistic model and validation: Geophysics, **81**, no. 2, E139–E157, doi: 10.1190/geo2015-0346.1.

Misra, S., C. Torres-Verdín, A. Revil, J. Rasmus, and D. Homan, 2016b, Interfacial polarization of disseminated conductive minerals in absence of redox-active species — Part 2: Effective electrical conductivity and dielectric permittivity: Geophysics, **81**, no. 2, E159–E176, doi: 10.1190/geo2015-0400.1.

Pelton, W. H., S. H. Ward, P. G. Hallof, W. R. Sill, and P. H. Nelson, 1978, Mineral discrimination and removal of inductive coupling with multifrequency IP: Geophysics, **43**, 588–609, doi: 10.1190/1.1440839.

Revil, A., 2013a, On charge accumulations in heterogeneous porous materials under the influence of an electrical field: Geophysics, **78**, no. 4, D271–D291, doi: 10.1190/GEO2012-0503.1.

Revil, A., 2013b, Effective conductivity and permittivity of unsaturated porous materials in the frequency range 1 mHz–1 GHz: Water Resources Research, **49**, 306–327, doi: 10.1029/2012WR012700.

Revil, A., G. Z. Abdel Aal, E. A. Atekwana, D. Mao, and N. Florsch, 2015b, Induced polarization response of porous media with metallic particles — Part 2. Comparison with a broad database of experimental data: Geophysics, **80**, no. 5, D539–D552, doi: 10.1190/geo2014-0578.1.

Revil, A., E. Atekwana, C. Zhang, A. Jardani, and S. Smith, 2012, A new model for the spectral induced polarization signature of bacterial growth in porous media: Water Resources Research, **48**, W09545, doi: 10.1029/2012WR011965.

Revil, A., A. Coperey, D. Mao, F. Abdulsamad, A. Ghorbani, M. Rossi, and D. Gasquet, 2018, Induced polarization response of porous media with metallic particles — Part 8: Influence of temperature and salinity: Geophysics, **83**, no. 6, E435–E456, doi: 10.1190/geo2018-0089.1.

Revil, A., A. Coperey, Z. Shao, N. Florsch, I. L. Fabricius, Y. Deng, J. R. Delsman, P. S. Pauw, M. Karaoulis, P. G. B. de Louw, E. S. van Baaren, W. Dabekaussen, A. Menkovic, and J. L. Gunnink, 2017b, Complex conductivity of soils: Water Resources Research, **53**, 7121–7147, doi: 10.1002/2017WR020655.

Revil, A., N. Florsch, and D. Mao, 2015a, Induced polarization response of porous media with metallic particles — Part 1: A theory for disseminated semiconductors: Geophysics, **80**, no. 5, D525–D538, doi: 10.1190/geo2014-0577.1.

Revil, A., A. Ghorbani, D. Jougnot, and B. Yven, 2023a, Induced polarization of clay-rich materials — Part 1: The effect of desiccation: Geophysics, **88**, no. 4, MR195–MR210, doi: 10.1190/geo2022-0510.1.

Revil, A., A. Ghorbani, D. Jougnot, B. Yven, D. Grgic, F. Bretaudeau, and J. Deparis, 2023b, Induced polarization of clay-rich materials — Part 2: The effect of anisotropy: Geophysics, **88**, no. 6, MR305–MR322, doi: 10.1190/geo2022-0511.1.

Revil, A., M. Le Breton, Q. Niu, E. Wallin, E. Haskins, and D. M. Thomas, 2017a, Induced polarization of volcanic rocks. 2. Influence of pore size and permeability: Geophysical Journal International, **208**, 814–825, doi: 10.1093/gji/ggw382.

Revil, A., D. Mao, Z. Shao, M. F. Sleevi, and D. Wang, 2017c, Induced polarization response of porous media with metallic particles — Part 6. The case of metals and semi-metals: Geophysics, **82**, no. 2, E97–E110, doi: 10.1190/geo2016-0389.1.

Revil, A., P. Vaudelet, Z. Su, and R. Chen, 2022, Induced polarization as a tool to assess mineral deposits: A review: Minerals, **12**, 571, doi: 10.3390/min12050571.

Schlumberger, C., 1920, Study of underground electrical prospecting, https://archive.org/details/studyofundergrou00schlrich/page/n21/mode/2up, accessed 12 June 2021.

Tartrat, Y. T., A. Revil, F. Abdulsamad, A. Ghorbani, D. Jougnot, A. Coperey, B. Yven, and R. de la Vaissière, 2019, Induced polarization response of porous media with metallic particles — Part 10. Influence of desiccation: Geophysics, **84**, no. 5, E357–E375, doi: 10.1190/geo2019-0048.1.

Wong, J., 1979, An electrochemical model of the induced polarization phenomenon in disseminated sulfide ores: Geophysics, **44**, 1245–1265, doi: 10.1190/1.1441005.

Wu, C., C. Zou, C. Peng, Y. Liu, T. Wu, J. Zhou, and C. Tao, 2022, Numerical simulation study on the relationships between mineralized structures and induced polarization properties of seafloor polymetallic sulfide rocks: Minerals, **12**, 1172, doi: 10.3390/min12091172.

Zanetti, C., A. Weller, M. Vennetier, and P. Mériaux, 2011, Detection of buried tree root samples by using geoelectrical measurements: A laboratory experiment: Plant Soil, **339**, 273–283, doi: 10.1007/s11104-010-0574-0.

Zhdanov, M. S., V. Burtman, M. Endo, and G. A. Wilson, 2012, Laboratory-based GEMTIP analysis of spectral IP data for mineral discrimination: 82nd Annual International Meeting, SEG, Expanded Abstracts, doi: 10.1190/segam2012-1268.1.

Zimmermann, E., J. Berwix, W. Glaas, H. Meier, H. M. Münch, and A. Kemna, 2007, ZEL-SIP04-V02: User manual: Forschungszentrum Julich GmbH.

Zimmermann, E., A. Kemna, J. Berwix, W. Glaas, H. M. Münch, and J. A. Huisman, 2008, A high-accuracy impedance spectrometer for measuring sediments with low polarizability: Measurement Science and Technology, **19**, 105603, doi: 10.1088/0957-0233/19/10/105603.

Biographies and photographs of the authors are not available.